Supplementary Information for

Elucidating inter-protein energy transfer dynamics within the antenna network from purple bacteria

Dihao Wang, Olivia C. Fiebig, Dvir Harris, Hila Toporik, Yi Ji, Chern Chuang, Muath Nairat, Ashley L. Tong, John I. Ogren, Stephanie M. Hart, Jianshu Cao, James N. Sturgis, Yuval Mazor, and Gabriela S. Schlau-Cohen

Gabriela S. Schlau-Cohen
E-mail: gssc@mit.edu

This PDF file includes:

Supporting Information Text

Materials and Methods

1.1 Preparation of LH2 and LH3. Wild-type *Ph. molischianum* DSM119 and DSM120 were grown as described previously with minor modifications (1). Briefly, 1000 mL of Hutner's media was degassed with nitrogen for one hour in a 1-L bottle, sealed with an open cap and silicone septum, and autoclaved for 20 min. Media was cooled to room temperature and inoculated with a live-growing bacterial culture. To produce LH2, the flask containing DSM119, which only produces LH2, was placed in front of a 70 W tungsten lamp, resulting in high-light and warm (30 ℃) temperature conditions. To produce LH3, the flask containing DSM120, which can produce both LH2 and LH3, was covered with a white paper napkin and placed further away from the tungsten lamp to create low-light and cool (23 ℃) temperature conditions. Several rounds of inoculating new culture were required for DSM120 to fully convert to LH3 production from LH2. Purification was performed according to previous protocols (1, 2) using n-dodecyl-β-D-maltoside (DDM) as the detergent.

1.2 Preparation of ApoE422K Belting Protein and Lipids. The belting protein ApoE422K used for doubly-loaded nanodisc samples was produced similarly to previously reported protocols for belting protein purification with modifications (2, 3). The plasmid (DNA 2.0) contained a thioredoxin fusion protein to improve belting protein expression, a thrombin cleavage sequence, a 6xHis tag, and kanamycin antibiotic resistance. A 10 mL starter culture of Luria Bertani Broth was inoculated with the glycerol stock and grown overnight in an incubator/shaker at 37 ℃, 180 rpm. The starter culture was used to inoculate 1 L of terrific broth. Protein overexpression was induced between 0.6 and 0.8 OD at 600 nm with a final concentration of 1 mM isopropyl-β-D-1-thiogalactopyranoside. Overexpression occurred for five hours. The cell pellet was collected by centrifuging for 20 min at 4000 rpm, 4 ℃ and then resuspended in 25 mL of 20 mM Tris, 150 mM NaCl, 1 mM MgCl$_2$, pH 7.4. The following were added to the resuspension: phenylmethylsulfonyl fluoride to a final concentration of 1 mM, Triton X-100 to a final concentration of 0.1% v/v, and 10 μL (20 units) of DNase I (New England Biolabs). The solution was homogenized in a Dounce tissue homogenizer and then probe sonicated on ice for five minutes at 30% power, 30 seconds on and 30 seconds off. The lysate was centrifuged for one hour at 4000 rpm, 4 ℃ to remove cellular debris, and the supernatant was loaded onto a 25-mL Ni-NTA column. The sample was incubated on the column overnight on a nutating mixer at 4 ℃. Purification was performed by washing with three column volumes each of 40 mM Tris HCl, 300 mM NaCl, 1% Triton-X 100, pH 8.0, 40 mM Tris HCl, 300 mM NaCl, 20 mM imidazole, 50 mM Na Cholate pH 8.0, 40 mM Tris HCl, 300 mM NaCl, 50 mM imidazole pH 8.0, 40 mM Tris HCl, 300 mM NaCl, 100 mM imidazole pH 8.0, and 40 mM Tris HCl, 300 mM NaCl, 400 mM imidazole pH 8.0. The fractions containing ApoE422K were combined and dialyzed in 1 L 20 mM Tris, 100 mM NaCl, 0.5 mM EDTA, pH 7.4 with three buffer changes every eight hours. 100 uL (1000 units) of TEV protease (New England Biolabs) were added to the sample and incubated overnight at 4 ℃ on a nutating mixer to simultaneously cleave the histidine tag and the thioredoxin fusion protein. The TEV, cleaved fusion protein, and histidine tag were removed by loading the sample on a 25-mL Ni-NTA column that was incubated overnight, ensuring that the TEV, cleaved fusion protein, and histidine tag were bound to the column. The purified, cleaved ApoE422K was collected by washing the column with 20 mM Tris HCl, 150 mM NaCl, pH 7.4. The TEV, cleaved fusion protein, and histidine tag were removed from the column by washing with 40 mM Tris HCl, 300 mM NaCl, 400 mM imidazole, pH 8.0.

The powdered form of 1,2-dimyristoyl-sn-glycero-3-phosphocholine (DMPC) was purchased from Avanti Polar lipids. A 100 mM stock solution was prepared by dissolving in 20 mM Tris-HCl, 150 mM NaCl, 100 mM Na Cholate, pH 7.5, and sonicated in a bath for one hour. The stock solution was prepared fresh for each preparation of nanodiscs.

1.3 Assembly of DLDs. Nanodiscs loaded with LH2 and LH3 were produced using the belting protein ApoE422K, which is a 22 kDa fragment of apolipoprotein E4. DMPC was used as the lipid. ApoE422K, LH2, LH3, and DMPC were mixed together in a molar ratio of 1:0.125:0.125:22.2 for small DLDs and 1:0.125:0.125:30 for large DLDs. These ratios were chosen to maximize the number of doubly-loaded nanodiscs produced, as at these ratios theoretically 100% of nanodiscs produced would contain two proteins. The reaction mixture was produced by adding each of the following in this order: lipid (DMPC), LH2, LH3, buffer (20 mM Tris HCl, 150 mM NaCl, pH 7.5), protease inhibitor cocktail (5 μL), and belting protein (ApoE422K). The belting protein was added last to prevent premature formation of nanodiscs. The reaction was incubated on a rocker for one hour at room temperature. Bio-Beads SM-2 Resin (Bio-Rad Laboratories) were added to 2/3 the volume of the reaction and incubated on a rocker for five hours at room temperature and then overnight at 4 ℃ on a nutating mixer.

The nanodiscs were purified by fast protein liquid chromatography (FPLC) on a BioRad NGC Chromatography system (Bio-Rad Laboratories) on a Superdex 200 Increase 10/300 GL (Cytiva) (Fig. S2). The flow rate was 0.4 mL/min and the buffer used was 20 mM Tris HCl, 150 mM NaCl, pH 7.5. The FPLC peaks were characterized by linear absorption, SDS-PAGE, and transmission electron microscopy (TEM) to identify the fractions that contained LH2-LH3 DLDs.

1.4 Negative Stain TEM Sample Preparation and Measurements. Nanodisc samples were prepared for TEM on negatively glow-discharged 400-mesh Cu–carbon coated films (Electron Microscopy Sciences). 5 μL of sample was deposited onto the grid for one minute and then the excess was removed using Whatman filter paper. 5 μL of a 2% (w/v) uranyl acetate solution in water was added to the grid for 30 seconds and the excess stain was removed. Samples were allowed to air dry for at least one hour before being imaged on an FEI Tecnai (G2 Spirit TWIN) at 120 kV at the MIT Materials Research Laboratory (MRL) Shared Experimental Facilities.

1.5 Sample preparation for single-particle cryo-EM analysis. Calculation of the correct concentration of membrane-discs for cryo-EM was done as follows. LH2 and LH3 are 88,303 Da, each. ApoE422K is 21,943 Da. A single DMPC lipid is 678 Da. The ratio of membrane-disc components determined by optimization of membrane-disc reactions is 2 light-harvesting complexes, 8 ApoE422K belting proteins, and 178 or 240 DMPC molecules for small and large DLDs, respectively. Overall, these DLDs amount to a total weight of 472,834 and 514870 Da, for small and large DLDs, respectively. Concentration of nanodiscs was found by identifying the concentration of LH2 by the absorption of the B850 band. That concentration and the molecular weight of the whole disc were used to find the membrane-disc concentration in mg/mL. A nanodisc concentration of 0.75 to 1 mg/mL was optimal for data collection. The sample was deposited on a gold standard R 1.2/1.3 holey carbon grids 300 mesh (Quantifoil) and vitrified by flash-plunging the grid into liquid ethane using an automated plunge freezer, a Vitrobot MarkIV (ThermoFisher/FEI) with a blotting time of 5 s and a blot force of 5.

1.6 CryoEM data acquisition and processing. The cryo-EM specimens were imaged on a Titan Krios transmission electron microscope (ThermoFisher/FEI). Electron images were recorded using a Falcon III direct electron detect camera (FEI) at super-resolution counting mode. The nominal magnification was ×92,000, corresponding to a super-resolution pixel size of 0.1599 Å at the specimen level. The counting rate was adjusted to 19.37 e$^-$/px/s. Total exposure time was 7.00s, accumulating to a dose of 54.56 e$^-$/Å^2.

Data processing was carried out with Relion 3.0 suite (4). Relion implementation of MotionCorr was used to register the translation of each sub-frame. Contrast transfer function parameters for each movie were determined using CTFFIND4 (5). Autopicking using LoG resulted in 1706944 particles, which were then 2D classified in an unsupervised manner, without alignment. Of those, 366361 particles clustered into 23 classes, which were then picked to either the parallel or the anti-parallel cascades. 3D reconstructions of anti-parallel and parallel reference maps were used to perform 3D classification. This procedure yielded classes which clearly showed the parallel (59893 particles) and anti-parallel (105458 particles) orientations. Several further rounds of 2D classification resulted in the final sets which contained 28771 parallel and 71566 anti-parallel particles. Three-dimensional reconstructions of parallel and anti-parallel orientations using these sets yielded volumes at a resolution of 11.1Å and 8.2Å, respectively. Lastly, high-resolution crystal structures of *Ph. molischianum* LH2 (PDB Code 1LGH) devoid of all amino acids side chains and containing BChla rings only were used to dock into the cryoEM map. LH3 was modeled by mutating the respective residues in 1LGH and removing their side chains. Both models were docked into cryoEM maps as rigid bodies in ChimeraX (6).

The maps and models were deposited on the PDB and EMDB with the following accession codes: small nanodisc parallel orientation: PDBID 7TV3, EMD-26138. Small nanodisc anti-parallel: PDBID 7TUW, EMD-26134, large nanodisc parallel orientation: PDBID 8FBB, EMD-28963, large nanodisc anti-parallel orientation: PDBID 8FB9, EMD28962.

1.7 Steady-State Spectra and Lifetime Measurements. Linear absorption spectra were recorded using an Epoch microplate spectrophotometer (BioTek) on the purified nanodisc samples. The absorption measurements were repeated after the TA experiments to confirm the absence of any sample degradation. The steady-state fluorescence measurements were taken using a home-built fluorescence setup with 532 nm excitation, an 600 nm 50 g/mm grating, and a PIXIS CCD camera (Princeton Instruments) (7). The steady-state absorption and fluorescence spectra of detergent-solubilized LH2/LH3 and DLDs samples (LH2-LH2 DLDs, LH3-LH3 DLDs, and LH2-LH3 DLDs) were measured (Figs. S5-S7). In addition, the steady-state spectra of three mixture samples with different percentages of LH2-LH2 and LH3-LH3 DLDs were also measured (Fig. S8). Due to the stochastic nature of nanodisc assembly, the LH2-LH3 DLDs sample contains three subpopulations.

$$P(LH22) + P(LH23) + P(LH33) = 1 \tag{1}$$

where P is the subpopulation percentage. Spectral decomposition analysis was applied to determine the subpopulation percentages. Specifically, the steady-state spectra of the LH2-LH3 DLDs and mixture samples were decomposed into LH2-LH2 DLDs and LH3-LH3 DLDs components (Fig. S8A,B). The results are shown as the relative absorbance $\frac{Abs(LH22,800nm)}{Abs(LH33,800nm)}$ and the relative integrated fluorescence $\frac{Int.fluorescence(LH22)}{Int.fluorescence(LH33)}$ in Figs. S8C and D. Since each LH2-LH3 disc contains one LH2 and LH3 complex, the absorption spectra decomposition of the LH2-LH3 DLDs sample can be expressed as follows:

$$\frac{Abs(LH22,800nm)}{Abs(LH33,800nm)} = \left(\frac{P(LH22) + 0.5P(LH23)}{P(LH33) + 0.5P(LH23)} \right) \cdot \frac{\varepsilon(LH22,800nm)}{\varepsilon(LH33,800nm)} \tag{2}$$

where ε is the extinction coefficient. The percentages of individual LH2 (a) and LH3 (b) complexes present in the LH2-LH3 DLDs sample can be calculated based on the relative absorbance (Table S4). Subsequently, the theoretical percentage of each subpopulation can now be determined ($a \cdot a$, $2a \cdot b$, and $b \cdot b$ for LH2-LH2, LH2-LH3, and LH3-LH3 DLDs, respectively). For the measured fluorescence spectra, we have:

$$\int_0^{+\infty} I_0(\lambda)d\lambda = \int_0^{+\infty} I_{\text{LH22}}(\lambda)d\lambda + \int_0^{+\infty} I_{\text{LH23}}(\lambda)d\lambda + \int_0^{+\infty} I_{\text{LH33}}(\lambda)d\lambda \tag{3}$$

where $I_0(\lambda)$ is the total steady-state fluorescence of LH2-LH3 DLDs sample and $\int_0^{+\infty} I(\lambda)$ is the integrated fluorescence area. The steady-state fluorescence ($I(\lambda)$) is the time integral of the fluorescence decay (8). When the excited-state dynamics of each

subpopulation be approximated as mono-exponential, we have:

$$I_{\text{LH22}}(\lambda) = K \cdot I_0(\lambda) \int_0^{+\infty} F_{\text{LH22}}(\lambda)[LH22(t)]dt \qquad\qquad [LH22(t)] = [LH22]_{\text{t}=0} \exp\left(-k_{\text{LH22}}t\right) \qquad [4]$$

$$I_{\text{LH23}}(\lambda) = K \cdot I_0(\lambda) \int_0^{+\infty} F_{\text{LH23}}(\lambda)[LH23(t)]dt \qquad\qquad [LH23(t)] = [LH23]_{\text{t}=0} \exp\left(-k_{\text{LH23}}t\right) \qquad [5]$$

$$I_{\text{LH33}}(\lambda) = K \cdot I_0(\lambda) \int_0^{+\infty} F_{\text{LH33}}(\lambda)[LH33(t)]dt \qquad\qquad [LH33(t)] = [LH33]_{\text{t}=0} \exp\left(-k_{\text{LH33}}t\right) \qquad [6]$$

where K is a normalizing factor, $[LH22(t)]$, $[LH23(t)]$, and $[LH33(t)]$ are the kinetics of excited DLDs, $[LH22]_{\text{t}=0}$, $[LH23]_{\text{t}=0}$ and $[LH33]_{\text{t}=0}$ are the initial populations. $F(\lambda)$ is the fluorescence intensity per unit population per unit time, which has the shape of the steady-state fluorescence spectrum. Since the absolute values of τ_{LH23} and $F_{\text{LH23}}(\lambda)$ cannot be directly measured, in this analysis we assume that nearly all the LH2-LH3 subpopulation exhibit LH2 fluorescence ($F_{\text{LH23}}(\lambda) \propto F_{\text{LH22}}(\lambda)$, $\tau_{\text{LH22}} = \tau_{\text{LH23}}$), and the intra-protein energy transfer dynamics and efficiencies are the same for LH2 and LH3 complex. The relative integrated fluorescence can be written as:

$$\frac{Int.fluorescence(LH22)}{Int.fluorescence(LH33)} = \frac{\int_0^{+\infty} I_{\text{LH22}}(\lambda)d\lambda + \int_0^{+\infty} I_{\text{LH23}}(\lambda)d\lambda}{\int_0^{+\infty} I_{\text{LH33}}(\lambda)d\lambda} \qquad [7]$$

Given the fact that the number of initially excited DLDs is proportional to absorbance ($[LH]_{\text{t}=0} \propto P(LH) \cdot \varepsilon$), Eq. (4-7) can be combined with population percentages as variables. Consequently, the subpopulation percentages can be determined with three equations (1), (2), and (7). The results are summarized in Table S4. Furthermore, the spectral decomposition results of the mixture samples were analyzed similarly ($P[LH23] = 0$). Based on the above supplementary equations, the relative absorbance and relative integrated fluorescence are directly proportional:

$$\frac{Int.fluorescence(LH22)}{Int.fluorescence(LH33)} = m \cdot \frac{Abs(LH22, 800nm)}{Abs(LH33, 800nm)} \qquad [8]$$

The m values are shown in Fig. S8C and D. The results of all three mixture samples show good linearity, further validating the consistency of our DLDs sample preparation and the analysis method's applicability to the DLDs spectra data. The results are shown in Table S4.

The fluorescence lifetime measurements were carried out using time-correlated single-photon counting (TCSPC) and fit as described previously (1, 2). The excitation wavelength was selected with a 790 nm 10-nm bandpass filter (FB790-10, Thorlabs, NJ). The fluorescence wavelength was selected with an 860 nm bandpass filter (FB860-10, Thorlabs, NJ). The excitation density was 10 μW/cm^2. The instrument response function (IRF) was 76 ps (Fig. S9).

1.8 Sample Preparation for Ultrafast Spectroscopy. After purification, the nanodiscs were diluted to ~1.5 OD at a 1 cm path length at 850 nm in 20 mM Tris, 150 mM NaCl, pH 7.4. The sample was flowed using a peristaltic pump and stored on ice during data acquisition.

1.9 Transient Absorption Spectroscopy. The transient absorption (TA) setup consists of a regeneratively amplified Ti:Sapphire laser (Libra, Coherent, Santa Clara, CA) producing femtosecond pulses centered around 800 nm at a repetition rate of 5 kHz. The output was split into two arms, one arm was used directly as the pump and the other arm was sent into an Ar-filled tube to generate a white-light continuum. The white-light arm was used as a probe after it was spectrally filtered between 700-900 nm and compressed using a pair of prisms. The pump arm was modulated at 2.5 kHz using an optically-gated chopper and then sent into an optical delay line and a half-wave plate to set its relative polarization at magic angle. The pump energy was set to 6 μJ/cm^2, which is well below the exciton-exciton annihilation threshold in LH2 (9). Both arms were non-collinearly combined and focused using achromatic lenses with a 30.0 cm focal length into a flow cuvette with a 1 mm optical path. The probe arm was collected using a home-built Czerny-Turner spectrograph and was detected with a CCD array (Aviiva EM2, Teleydyne e2v) on a shot-to-shot basis. Each two consecutive laser shots were used to calculate the TA spectrum at each delay point using $\Delta\text{TA} = \log(\text{pump off/pump on})$. For each scan, 2500 TA spectra were collected at each time delay across the TA trace and further traces were repeated and averaged until good signal-to-noise traces were obtained. The overall instrument response is determined to be 110 fs for the setup by measuring the coherent artifacts (10). Global and target analysis for the TA data was carried out using Glotaran software (11).

1.10 Kinetic Models and Data Analysis for Transient Absorption. The pump pulse at 800 nm selectively excites the B800 ring in LH2 and LH3. The TA data of detergent-solubilized samples were analyzed globally (Fig. S12). The timescales for intra-protein energy transfer in LH2 and LH3 are in good agreement with previously reported values (1). Due to the stochastic nature of nanodisc assembly, the LH2-LH3 DLDs sample is inherently heterogeneous, containing three DLDs subpopulations of LH2-LH2, LH2-LH3, and LH3-LH3 DLDs. In order to extract the timescales for the LH3-to-LH2 energy transfer dynamics, homogeneous DLDs samples of LH2-only and LH3-only DLDs were first prepared and investigated. Since in the homogeneous DLDs samples, the two complexes incorporated into the same nanodisc are spectrally indistinguishable, the inter-protein energy transfer

dynamics cannot be directly observed by TA. Instead, the TA data of the homogeneous samples were globally analyzed with the sequential model. For LH3-LH3 DLDs:

$$\frac{d[B800_{LH3}(t)]}{dt} = -k_1[B800_{LH3}(t)] \tag{9}$$

$$\frac{d[B820(t)]}{dt} = k_1[B800_{LH3}(t)] - k_2[B820(t)] \tag{10}$$

$$\frac{d[B820^{rel}(t)]}{dt} = k_2[B820(t)] - k_3[B820^{rel(t)}] \tag{11}$$

For LH2-LH2 DLDs:

$$\frac{d[B800_{LH2}(t)]}{dt} = -k_4[B800_{LH2}(t)] \tag{12}$$

$$\frac{d[B850(t)]}{dt} = k_4[B800_{LH2}(t)] - k_5[B850(t)] \tag{13}$$

$$\frac{d[B850^{rel}(t)]}{dt} = k_5[B850(t)] - k_6[B850^{rel}(t)] \tag{14}$$

where k_1 and k_4 are the rate constants of intra-protein energy transfer from the B800 band to the B820 band in LH3 and B850 band in LH2, respectively. k_2 and k_5 are the rate constants of relaxation in the lower bands, and k_3 and k_6 are the rate constants of lifetime decays. The SADS are shown in Figs. S13 and S14, and the timescales are listed in Table S5. The changes in the relaxation timescales and the SADS shapes/positions indicate that the nanodiscs of different sizes have distinct nanoconfinement effects on the light-harvesting antenna complexes. In the LH2-LH3 DLDs sample, the populations of each DLDs at time zero were determined from the absorption profiles at 800 nm. With the dynamic and spectral information obtained from the above homogeneous samples, the timescales for the LH3-to-LH2 energy transfer in the LH2-LH3 DLDs subpopulation can be solved by fitting the following equations:

$$\frac{d[B800_{LH3}(t)]}{dt} = -k_1[B800_{LH3}(t)] \tag{15}$$

$$\frac{d[B820(t)]}{dt} = k_1[B800_{LH3}(t)] - k_2[B820(t)] - k_7[B820(t)] \tag{16}$$

$$\frac{d[B820^{rel}(t)]}{dt} = k_2[B820(t)] - k_7[B820^{rel}(t)] \tag{17}$$

$$\frac{d[B800_{LH2}(t)]}{dt} = -k_4[B800_{LH2}(t)] \tag{18}$$

$$\frac{d[B850]}{dt} = k_4[B800_{LH2}(t)] + k_7[B820(t)] + k_7[B820^{rel}(t)] - k_5[B850(t)] \tag{19}$$

$$\frac{d[B850^{rel}]}{dt} = k_5[B850(t)] - k_6[B850^{rel}(t)] \tag{20}$$

where k_7 is the rate constant of energy transfer from the B820 components in LH3 to the B850 component in LH2 within the same nanodisc. The parallel and anti-parallel orientations have different inter-protein distances. For the small LH2-LH3 DLDs sample, since the difference in the inter-protein distance is only 0.5 Å, the same timescale for LH3-to-LH2 energy transfer was used in both orientations (Figs. S15 and S16). On the other hand, the inter-protein distances are different by ∼3 Å between the two orientations in the large LH2-LH3 DLDs, which, according to the theoretical calculations, results in distinct timescales for inter-protein energy transfer. Therefore, both the anti-parallel (85% of the total LH2-LH3 DLDs population) and parallel (15% of the total LH2-LH3 DLDs population) orientations were included in the fitting. The fitting results are shown in Fig. S15 and Table S5.

As an alternative method, TA spectral analysis was applied to access the inter-protein energy transfer timescales in the LH2-LH3 DLDs. Mixture samples consisting of the two homogeneous DLDs (LH2-LH2 DLDs and LH3-LH3 DLDs, around 1:1 ratio) were prepared and investigated by TA. The TA data of LH2-LH3 DLDs, homogeneous DLDs, and mixture samples were taken under the same experimental condition. At each time delay, the TA spectra of the LH2-LH3 DLDs and the mixture samples were linearly decomposed into the LH2-LH2 DLDs and LH3-LH3 DLDs components (a·$\Delta A_{LH3-LH3}$ + b·$\Delta A_{LH2-LH2}$), and the LH3-to-LH2 TA spectral ratios (a/b) were plotted (Fig. S17). Within the time window, the ratios of the mixture samples remained relatively constant, while the ratios of LH2-LH3 DLDs samples decreased with time, which revealed the timescales for the inter-protein energy transfer in the LH2-LH3 DLDs subpopulation (Fig. S17B,D). The TA spectral fitting results are shown in Figs. S18 and S19.

1.11 Theoretical Calculation Models and Methods. In this section we introduce the models accounting for the excitonic structure of LH2/LH3, as well as the generalized FRET formalism adopted to calculate the inter-protein excited state energy transfer rates.

1.11.1 Frenkel Exciton Models.

We aim at building a Frenkel exciton model for the B800-850 pigment protein complexes (LH2) from *Phaeosprillum molischianum* and that of the blue-shifted B800-820 complexes from the same organism grown under stress (LH3). Both of these complexes are octameric. We base the models on the parametrization by Chmeliov et al. (12), where a different purple bacterium, *Rhodoblastus acidophilus*, with nonameric LH2 and LH3 complexes were studied. Specifically, we adopt the on-site energies (moderately modified to better fit the linear absorption and emission spectra) and the short-range coupling terms from this model, and long-range (second neighbors and farther) couplings are calculated using transition monopole approximation (13, 14) based on the cryoEM structure. The transition monopoles (charges) corresponding to the ground and the first excited state (Q_y transition) of the BChla molecules are calculated using the ZINDO method implemented in Gaussian (15). The numerical values for the on-site energies and the couplings are listed in Tables S6 and S7. To account for the monomeric exciton nature of B800 BChlas (16), the intra-complex excitonic couplings between B800 BChlas are neglected. The resulting energy levels of LH2 and LH3 complexes are shown in Fig. S22.

The inter-complex couplings are also calculated using the transition monopole approximation, explicitly:

$$J_{12} = \sum_{i,j} \frac{q_i^{(1)} q_j^{(2)}}{\epsilon |\vec{r}_i^{(1)} - \vec{r}_j^{(2)}|} \tag{21}$$

where i (j) runs over all atoms of molecule 1 (2), q_i and $\vec{r}_i$ are the transition monopole and the position of the corresponding atoms, and ϵ is the vacuum permittivity. The values for transition monopoles are for the Q_y transition of BChla and are shown in Table S10.

1.11.2 Far-field Absorption and Emission Spectra.

In our simulations we assume a shifted Gaussian profile for the lineshape functions:

$$
\begin{aligned}
E_\mu(\omega) &= \frac{1}{\sqrt{2\pi\sigma_\mu^2}} \exp\left(-\frac{(\omega - \omega_\mu + \lambda_\mu)^2}{2\sigma_\mu^2}\right) \\
A_\nu(\omega) &= \frac{1}{\sqrt{2\pi\sigma_\nu^2}} \exp\left(-\frac{(\omega - \omega_\nu - \lambda_\nu)^2}{2\sigma_\nu^2}\right)
\end{aligned}
\tag{22}
$$

where ω_μ is the energy, σ_μ is the linewidth, and λ_μ is the reorganization energy of state μ. While the former is obtained from diagonalizing the Frenkel exciton Hamiltonian discussed in the previous section, the latter two are fitted from experimental spectra. Specifically, we assume a uniform reorganization energy for all states, $\lambda_\mu = \lambda_\nu = \lambda = 77.3$ (cm^{-1}), and the spectral widths for the B800 band and those of the B820/B850 band are set to $\sigma_{\text{B800}} = 217$ and $\sigma_{\text{B820}} = \sigma_{\text{B850}} = 271$ (cm^{-1}), respectively.

With the lineshape functions given above, we need the information of the transition dipole moments of the BChla molecules to calculate the far-field linear spectra, where the dipole approximation is invoked and is given by $\vec{\mu} = \sum_i q_i \vec{r}_i$. The far-field linear spectra can be expressed as follows.

$$E^{(\text{f})}(\omega) = \sum_{\mu=1}^{N_\text{d}} p_\mu f_\mu E_\nu(\omega)$$

$$A^{(\text{f})}(\omega) = \sum_{\nu=1}^{N_\text{a}} f_\nu A_\nu(\omega) \tag{23}$$

where $f_\mu = |\sum_{n=1}^{N} \phi_n^\mu \vec{\mu}_n|^2$ is the oscillator's strength for each excitonic state. The calculated spectra, alongside with the experimental ones, are shown in Fig. S23. The calculated spectra are generally agreeing with the experiment, with the exception of the high energy shoulders of absorption spectra that are attributed to Qx transitions of BChla. The low energy shoulders of experimental LH3 spectra are from the residual LH2 components.

1.11.3 Generalized FRET Rate.

To account for the near-field effect in estimating the excitonic energy transfer rate between two adjacent complexes, we adopt the generalized FRET (gFRET) formalism (16, 17). Here the energy transfer rate between a group of donor molecules, collectively excited in their one-exciton manifold, and a group of acceptor molecules is expressed as

$$k_{\text{ad}} = \frac{1}{2\pi\hbar^2} \int_{-\infty}^{\infty} dt \cdot \text{Tr}[\mathbf{J}^T \mathbf{E}^{(\text{d})}(t) \mathbf{J} \mathbf{A}^{(\text{a})}(t)] \tag{24}$$

where $\mathbf{J} = \sum_{m=1}^{N_\text{d}} \sum_{n=1}^{N_\text{a}} |m\rangle\langle n| J_{mn}$ is the matrix containing pairwise excitonic couplings between all N_d donor and N_a acceptor molecules. $\mathbf{E}^{(\text{d})}(t)$ and $\mathbf{A}^{(\text{a})}(t)$ are the matrices of the emission and absorption operators of the donor and acceptor molecules in the time domain, respectively. We refer the reader to ref.(17) for details. Further assuming the diagonal approximation in the energy eigenbasis, we arrive at

$$k_{\text{ad}} \approx \frac{1}{2\pi\hbar^2} \sum_{\mu=1}^{N_\text{d}} \sum_{\nu=1}^{N_\text{a}} p_\mu(T) |J_{\mu\nu}|^2 \int_{-\infty}^{\infty} d\omega \cdot E_\mu(\omega) A_\nu(\omega) \tag{25}$$

where $J_{\mu\nu}$ is the excitonic coupling matrix element between energy eigenstates μ of the donor group and ν of the acceptor group. $p_\mu(T) = e^{-\epsilon_\mu/k_B T}/Z$ is the Boltzmann population of donor state μ and $Z = \sum_\mu e^{-\epsilon_\mu/k_B T}$ is the partition function. $E_\mu(\omega)$ and $A_\nu(\omega)$ are the lineshape functions of the corresponding states. This approximation is appropriate when the temperature is high such that the contributions from inter-state coherence terms is weak.

The calculated value for the LH2→LH2 inverse rate is 56 ps. To better compare with experiment, the gFRET methodology under the same approximations (Gaussian lineshape, diagonal approximation) is applied to a different LH2 B850 system with known numerically exact result by Strumpfer and Schulten using the hierarchical equations of motion method (18). The exact result is 9.5 ps, compared to the approximated gFRET rate of 80 ps. Using this as a benchmark we estimate the true LH2-LH2 gFRET rate to be 6.6 ps. The calculated and rescaled energy transfer rates between two neighboring complexes in the parallel and the anti-parallel orientations, revealed by the cryoEM measurement, are tabulated in Figure S21.

1.11.4 Relative Rates. As reported in Figure S21, the gFRET rates between different types of LH complexes follow the following trend: LH3→LH3 ≈ LH3→LH2 > LH2→LH2 for both the parallel and the anti-parallel double ring orientations. The ordering of the latter three rates is expected due to the ordering of their respective energies, as the energy transfer is dominated by that between B850/B820→B850/B820 bands: Downhill transfer (B820, LH3→B850, LH2) is faster than the symmetric dimer (B850, LH2→B850, LH2).

In addition, the ordering of the two symmetric dimer cases LH3→LH3 > LH2→LH2 is attributed to the factor of donor thermal population, $p_\mu(T)$ in Eq. (25): In LH3, the energy separation between the B800 and B820 bands is 300 cm^{-1}, corresponding to 11% thermal population in the B800 band. In LH2, in contrast, the separation between B800 and B850 is 730 cm^{-1}, corresponding to only 3.5% thermal population in the B800 band. Adding to the fact that the pre-thermal averaged energy transfer rate is much higher between B800 bands than that between B850/B820 bands (see below), this gives rise to the slightly higher energy transfer rate between LH3s. This also explains the slow down of rates of LH3→LH2(3) for the anti-parallel orientations, since the B800 rings of the two complexes are farther separated compared to the parallel orientation, making the excitonic couplings between the two rings much smaller.

However, following the above analysis, one expects the case of LH3→LH2 to be of the fastest among the four pairs of combination. This is so since it benefits from a higher B820→B850 contribution as well as a higher B800→B800 contribution. While this is indeed the case, our result indicates that the LH3→LH2 rate is only on par with that of LH3→LH3. This is due to a reduction of B820 thermal population, in conjunction with the increase of B800 population that leads to higher B800→B800 rate. As a result, the gain in having a better spectral overlap between the B820 and B850 bands (compared to the symmetric B820/B820) is attenuated by the decrease in B820 thermal population.

We emphasize that the results reported in Figure S21 as well as the above analysis are limited by the approximations applied in the gFRET calculations and the uncertainty of the excitonic model parameters. In our experiment only the LH3→LH2 rate can be uniquely determined.

1.11.5 Distance Dependent Energy Transfer Rate. In this section we examine the dependence of the inter-complex energy transfer rate on the separation between the complexes. All rates irrespective of the underlying excitonic structures scale as R^{-6} as predicted by the Förster theory.

$$k_{ad}^{(F)}(R_{ad}) \propto p_d \kappa_{ad}^2 S_{ad} \frac{|\vec{\mu}_d|^2 |\vec{\mu}_a|^2}{R_{ad}^6} \tag{26}$$

where p_d is the donor population, $\kappa_{ad} = \hat{\mu}_a \cdot \hat{\mu}_d - 3(\hat{\mu}_a \cdot \hat{R}_{ad})(\hat{\mu}_d \cdot \hat{R}_{ad})$ is the orientation factor, S_{ad} is the spectral overlap, and $\vec{\mu}_a$, $\vec{\mu}_d$ are the transition dipole moments. In the large separation limit, one simply substitutes the transition dipole moments with those of the far-field bright states of each complex and sets p_d to be that of the thermal population of the donor bright states.

On the other hand, notice the choice to use the separation between the closest inter-complex B820/B850 BChla pair instead of the center-to-center distance. This allows a more transparent visualization of the correct limit in the short-range regime. As such, the dominant contribution to the inter-complex rate is that between the closest pair of BChla molecules. Consequently, one also recovers the R^{-6} scaling in the limit. Here, in contrast to the large separation limit, we replace the transition dipole moments in Eq.(26) with those of the closest donor-acceptor pair, as well as the donor population with that on the single donor molecule.

It should be noted that the vertical gap between the R^{-6} scalings of the two limits reflects the effective number of pigments participating in the energy transfer process in the Förster picture. Assuming that both κ_{ad} and S_{ad} are similar in both the small- and the large-separation limits, the primary difference between the two limits comes from the magnitudes of the transition dipole moments and the donor population. For LH2 and LH3 complexes this amounts to a ratio of $10^2 - 10^3$ between the two limits.

In the intermediate regime, the rate dependence on separation is milder than the R^{-6} scaling of the two limits. This is a consequence of both the two limits and the vertical gap between them, as discussed in the last paragraph. It should be noted that in all cases the rates in the naturally occurring systems fall under this regime.

1.12 Exciton Transportation Simulation. We simulated the excitation energy transfer dynamics between LH2 complexes using a hexagonal lattice model. A random LH2 on the lattice was selected in each simulation run as the starting point. The exciton lifetime was set as 1 ns. We only consider the exciton hopping between neighboring LH2s, and the hopping probability was

proportional to the energy transfer rates (ps^{-1}) of different distances. Three membrane organizations of different intercomplex distances were investigated. First, the intercomplex distances (edge-to-edge) were set at 3.5 nm. Then, 7.7% of the intercomplex distances were set as 2.5 nm, while the rest (92.3%) remained 3.5 nm. These closely packed LH2s were either randomly distributed (random arrangement) or formed a central cluster (cluster arrangement) on the lattice. To generate a weighted average case, a 3.42 nm (= 0.077*2.5nm + 0.923*3.5nm) intercomplex distance was created (uniform arrangement). For each different arrangement, the exciton transport distance was averaged for 30000 simulation trajectories. Furthermore, to cover all the possibilities, we examined the exciton hopping distances of 100 different random arrangements. The simulation results are shown in Figure 4C and Table S9.
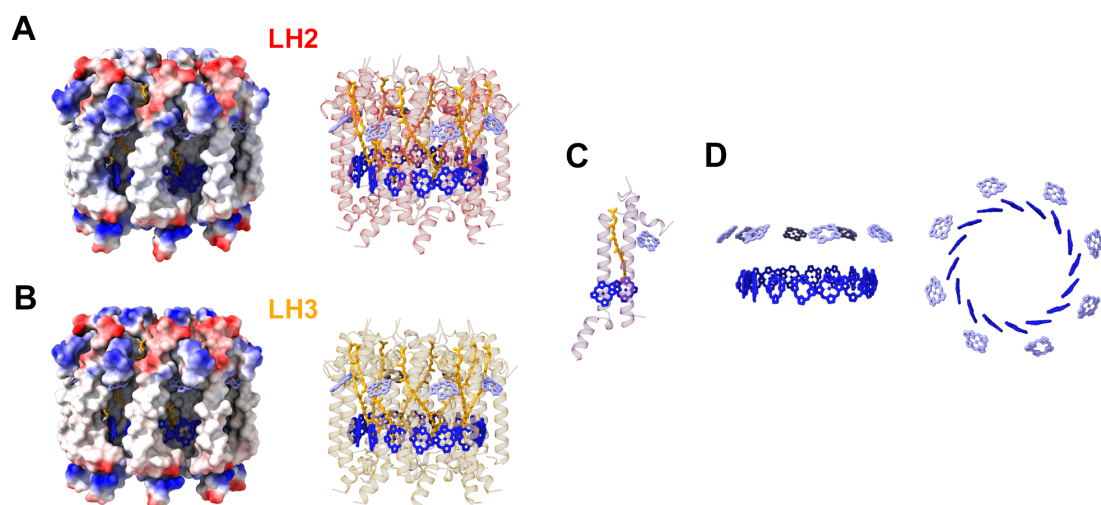
Fig. S1. Protein structures of (A) light-harvesting complex 2 (LH2) in *Ph. molischianum* (Protein Data Bank ID 1LGH) and (B) a homology model of its low-light variant, LH3, with surface charge densities (left) and structural organization (right). (C) Subunit of LH2. Each subunit is a heterodimer containing one B800 BChla (light purple), two B850 BChlas (blue), and one carotenoid molecule (yellow). (D) Side and top views of the B800 and B850 BChla rings.
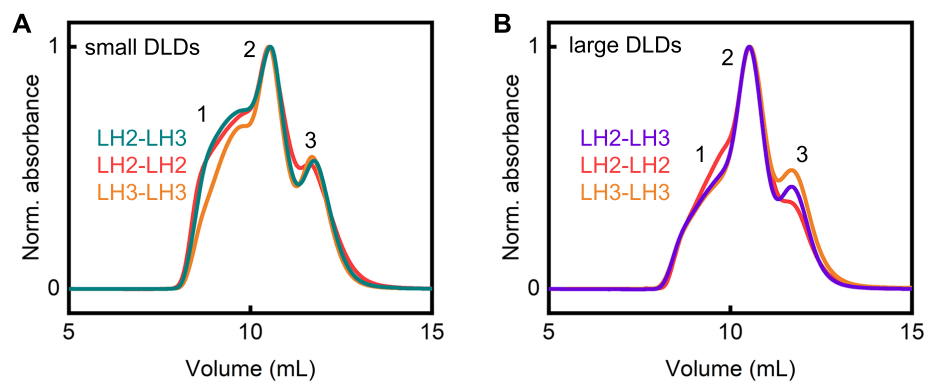
Fig. S2. Size-exclusion chromatography results of (A) small and (B) large DLDs samples. Peak 1 contains larger aggregates and peak 2 contains DLDs. Peak 3 contains free LH2 and singly-loaded nanodiscs. The center fractions of peak 2 were collected and used for further experiments.
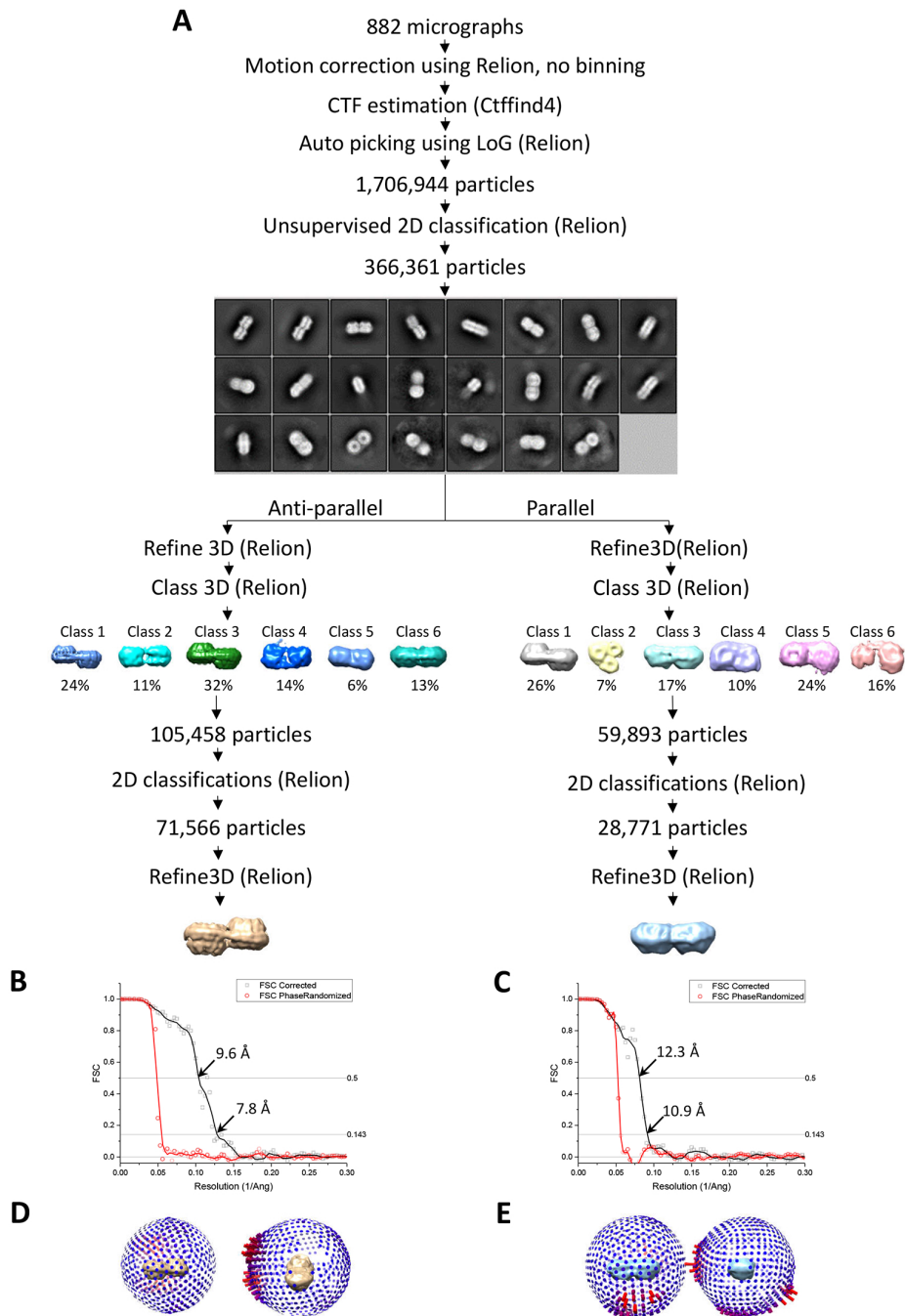
Fig. S3. CryoEM processing strategy for small DLDs. (A) Data collection and image processing strategy including selected 2D classes sorted by classes distribution and 3D classes. Further details can be found in the materials and methods section. (B) and (C) Plots of Fourier shell correlation (FSC) against resolution of the anti-parallel and parallel orientations, respectively. (D) and (E) Plots of Euler angle distribution of the anti-parallel and parallel orientations, respectively.

A

2250 micrographs
↓
Motion correction using Relion, no binning
↓
CTF estimation (Ctffind4)
↓
Auto picking using LoG (Relion)
↓
643,312 particles
↓
Unsupervised 2D classification (Relion)
↓
269,497 particles
↓

Class 1	Class 2	Class 3	Class 4	Class 5	Class 6
17.5 %	10.4 %	6.4 %	10.2 %	13.2 %	42.3 %

Anti parallel
194,105
↓
2D/3D classification
↓
63,637
Refine 3D (Relion4)

Parallel
34,524
↓
2D/3D classification
↓
11,133
Refine 3D (Relion4)

B   8.1 Å   6.4 Å
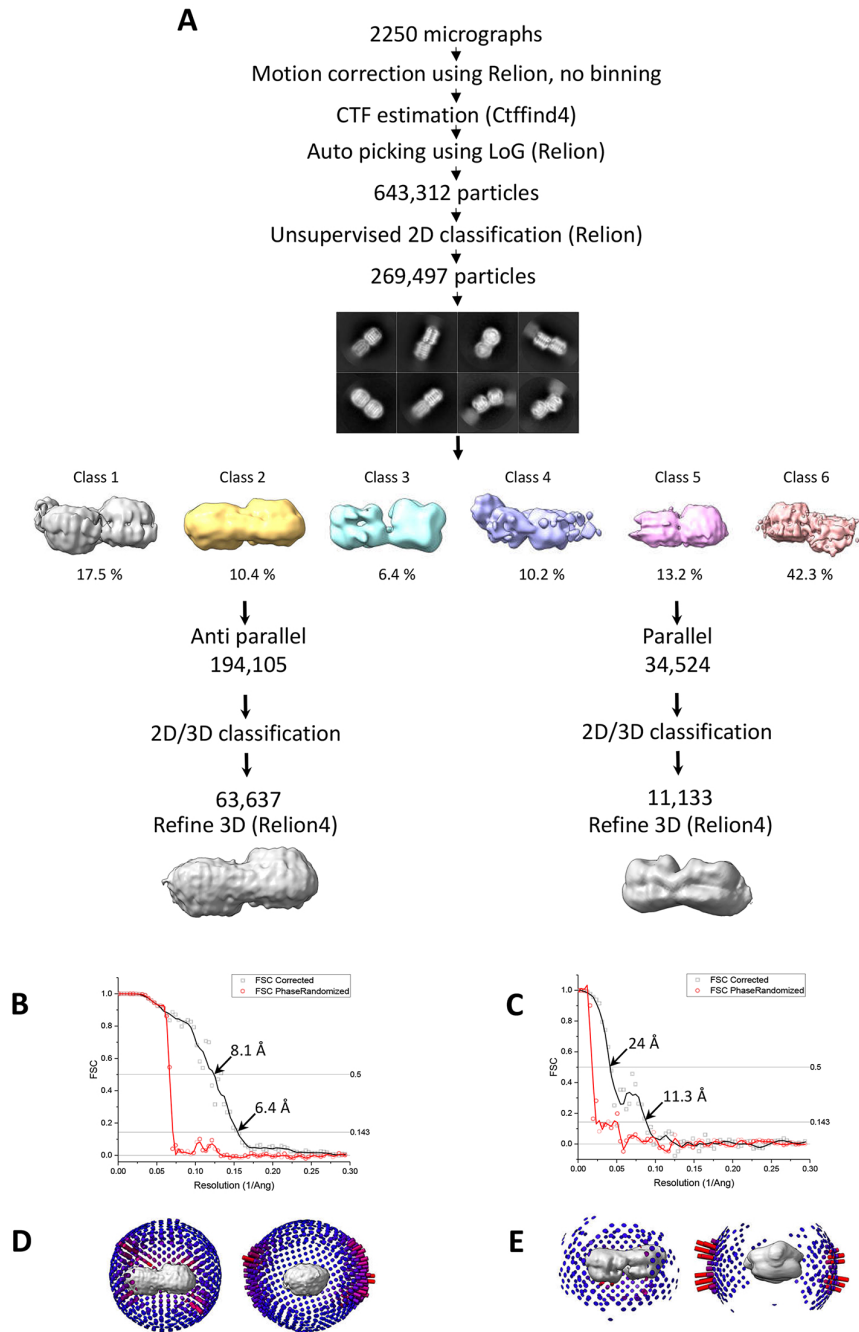
C   24 Å   11.3 Å

D

E

Fig. S4. CryoEM processing strategy for large DLDs. (A) Data collection and image processing strategy including selected 2D classes sorted by classes distribution and 3D classes. Further details can be found in the materials and methods section. (B) and (C) Plots of Fourier shell correlation (FSC) against resolution of the anti-parallel and parallel orientations, respectively. (D) and (E) Plots of Euler angle distribution of the anti-parallel and parallel orientations, respectively.
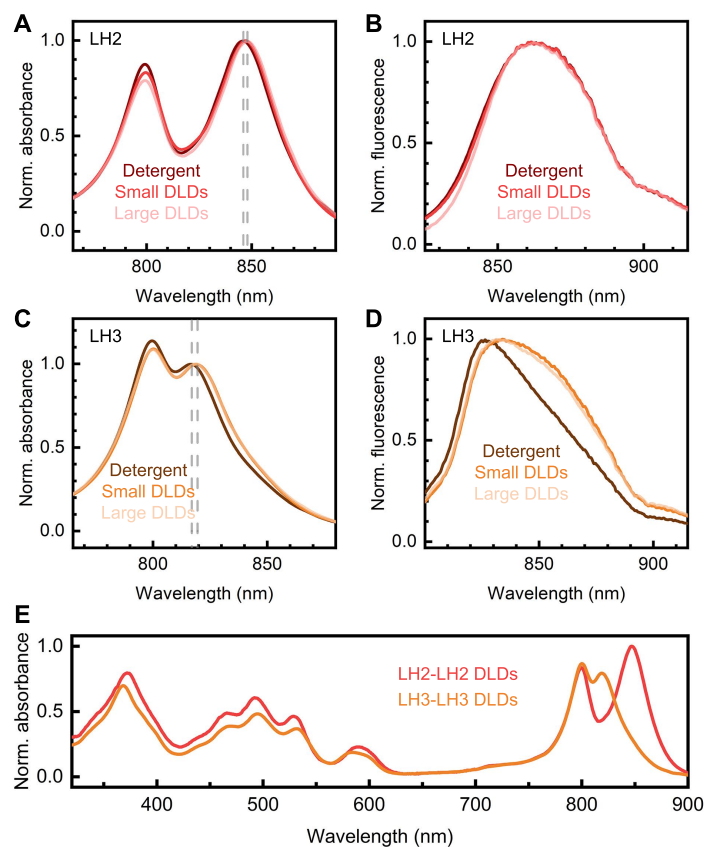
Fig. S5. Steady-state spectral comparisons. The (A) absorption and (B) fluorescence spectra of LH2 in detergent and DLDs. The (C) absorption and (D) fluorescence spectra of LH3 in detergent and DLDs. (E) UV-Vis absorption spectra of small LH2-LH2 and LH3-LH3 DLDs. The absorption peaks of lower bands are also shown with dashed lines and all peaks are summarized in Table S1.
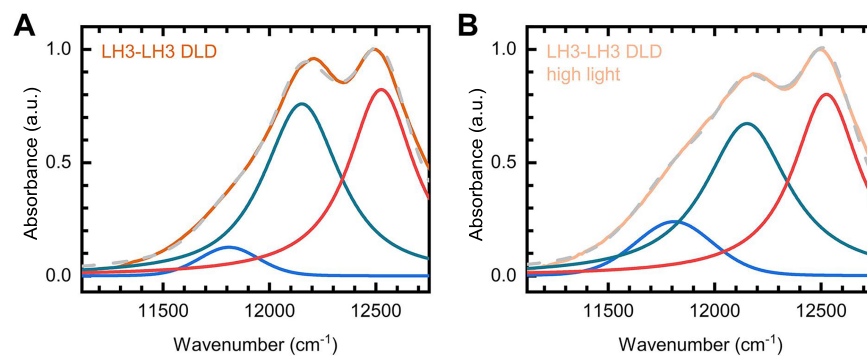
Fig. S6. Steady-state absorption spectra of LH3-LH3 DLDs from cells grown under (A) low light and (B) high light conditions. The absorption spectra are fitted with three pseudo-Voigt functions that represent the B800 (red), B820 (dark cyan), and B850 (blue) bands, respectively. The cumulative fits are shown as gray dashed lines. The full conversion from LH2 to LH3 has not been achieved in *Ph. molischianum*. The fitting results are listed in Table S2.
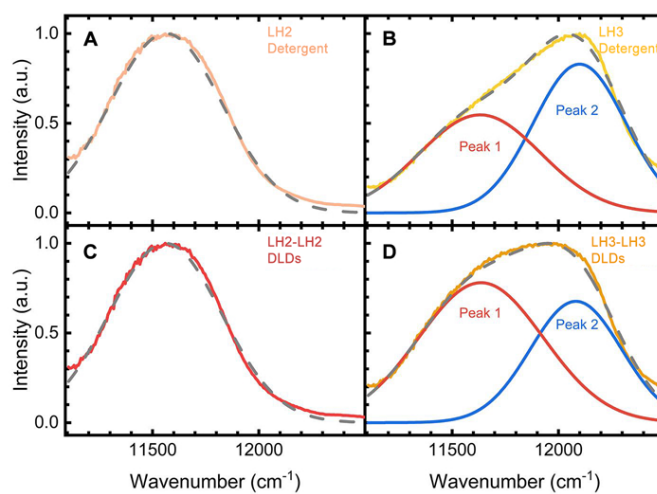
Fig. S7. Decomposition of LH2 and LH3 fluorescence spectra in (A,B) detergent and (C,D) small DLDs with Gaussian line shapes. The fitted spectra are shown as gray dashed lines. The fitting results are shown in Table S3.
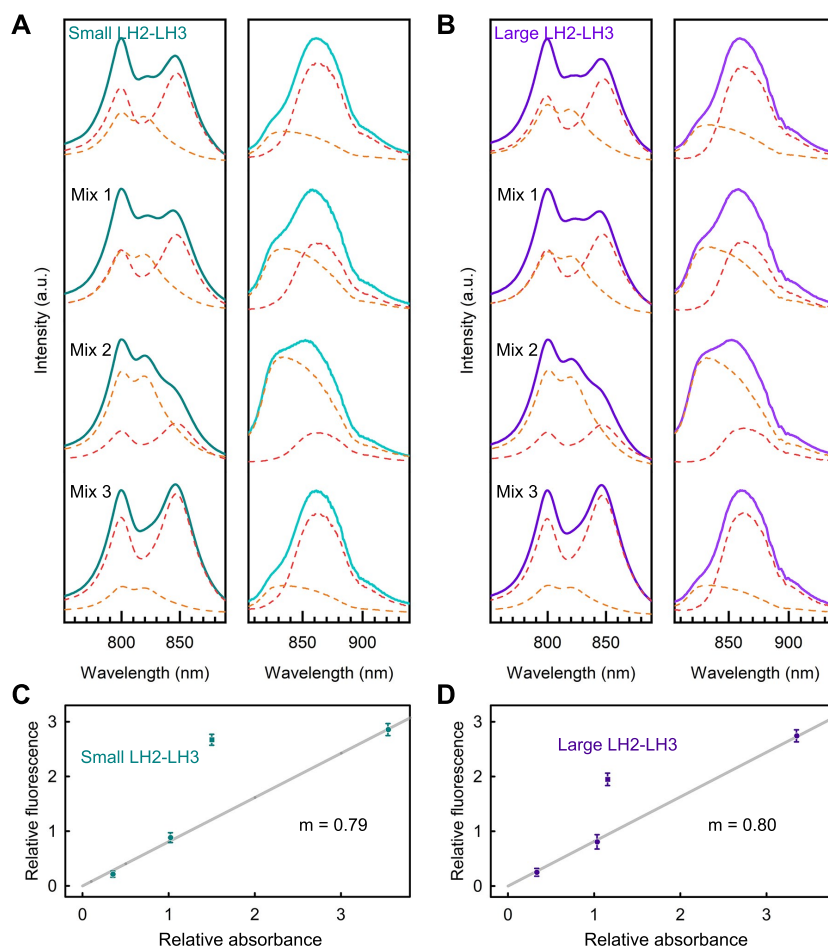
Fig. S8. Spectral decomposition analyses. The steady-state spectra of (A) small and (B) large DLDs samples. The LH2-LH3 DLDs samples contain three subpopulations of LH2-LH2 DLDs, LH3-LH3 DLDs, and LH2-LH3 DLDs, while the mixture samples contain different ratios of LH2-LH2 DLDs and LH3-LH3 DLDs. The LH2-LH2 DLDs components in the (left) absorption and (right) fluorescence spectra are shown in red, and the LH3-LH3 DLDs components are shown in orange. (C,D) Spectral decomposition of the LH2-LH3 DLDs and mixture samples. The analysis results are listed in Table S4.
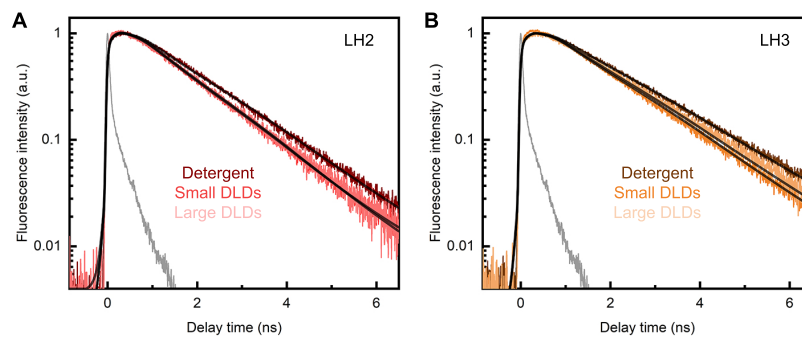
Fig. S9. Fluorescence dynamics of LH2 and LH3 in detergent and DLDs. Fluorescence decay traces at 860 nm for (A) LH2 and (B) LH3 samples were measured with time-correlated single photon counting. The fits are shown as black lines. The IRF is shown in gray. The fitting results are shown in Table S5.

Fig. S10. (A) LH2-LH3 DLDs absorption spectrum overlaid with the pump and probe spectra. (B) Example of coherent artifacts (black dots) and fitting (red line) at 845 nm.
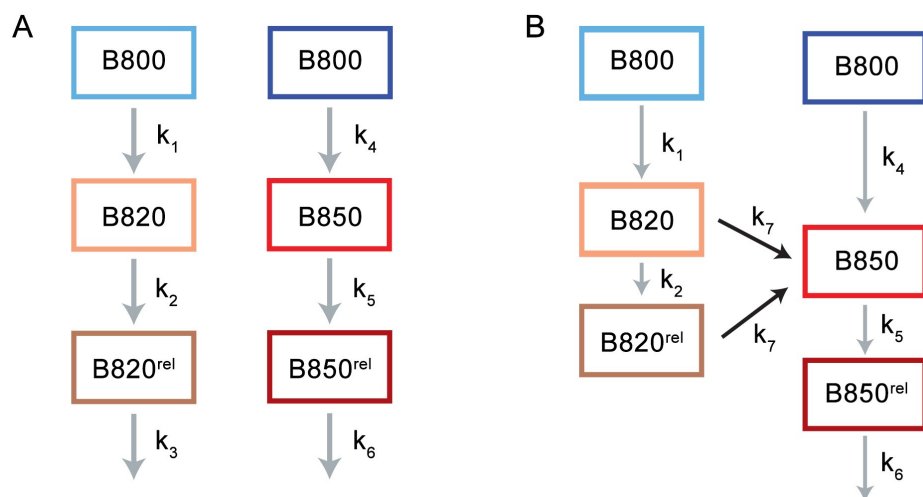
Fig. S11. Dynamic models of (A) LH2-LH2 and LH3-LH3 DLDs and (B) LH2-LH3 DLDs. The timescales are summarized in Table S5.

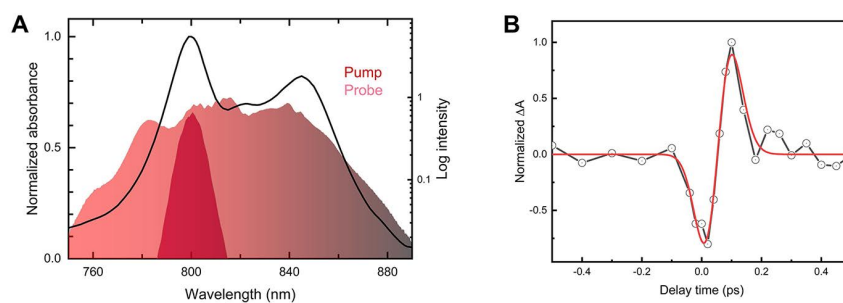Fig. S12. TA fitting results of detergent-solubilized samples. 2D representation of the femtosecond-resolved TA spectra of (A) LH3 and (D) LH2 in detergent. Color bar describes signal intensity (mOD). (B) SADS of B800 (gray) and B820 (orange) in LH3 and (E) SADS of B800 (gray) and B850 (red) in LH2. The SADS of LH2 and LH3 samples are normalized according to the negative peak of B850 and B820, respectively. (C,F) Absorption transients at selected wavelengths. All experimental data are shown as circles, and the best model fits are shown as lines. The timescales are shown in Table S5.

Fig. S13. TA fitting results of small DLDs samples. 2D representation of the femtosecond-resolved TA spectra of (A) LH3-LH3 DLDs and (D) LH2-LH2 DLDs. Color bar describes signal intensity (mOD). (B) SADS of B800, B820 and B820^{rel} in LH3 and (E) SADS of B800, B850 and B850^{rel} in LH2. The SADS of LH2-LH2 and LH3-LH3 DLDs samples are normalized according to the negative peak of B850 and B820, respectively. (C,F) Absorption transients at selected wavelengths. All experimental data are shown as circles, and the best model fits are shown as lines. The timescales are shown in Table S5.
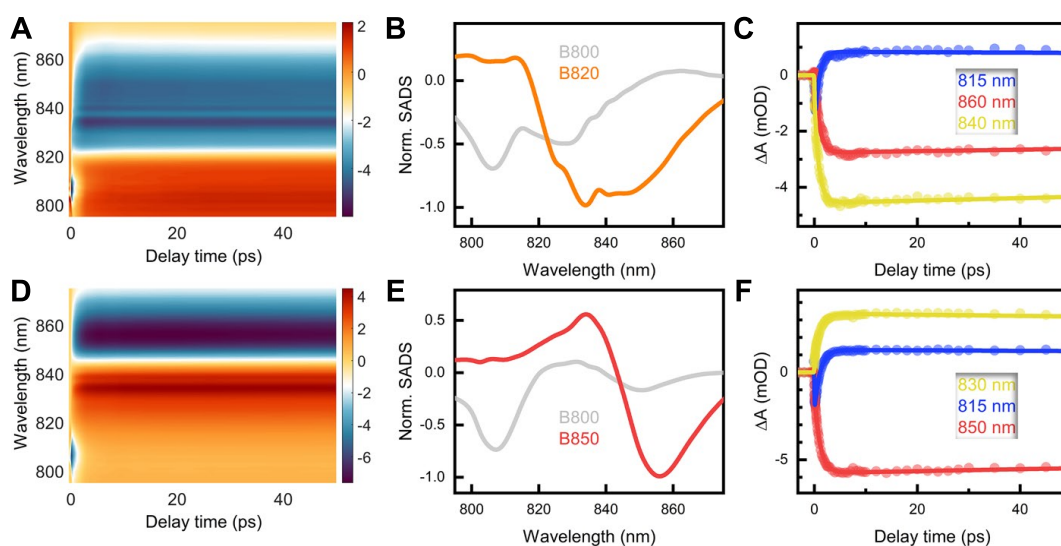
Fig. S14. TA fitting results of large DLDs samples. 2D representation of the femtosecond-resolved TA spectra of (A) LH3-LH3 DLDs and (D) LH2-LH2 DLDs. Color bar describes signal intensity (mOD). (B) SADS of B800, B820 and B820^{rel} in LH3 and (E) SADS of B800, B850 and B850^{rel} in LH2. The SADS of LH2-LH2 and LH3-LH3 DLDs samples are normalized according to the negative peak of B850 and B820, respectively. (C,F) Absorption transients at selected wavelengths. All experimental data are shown as circles, and the best model fits are shown as lines. The timescales are shown in Table S5.
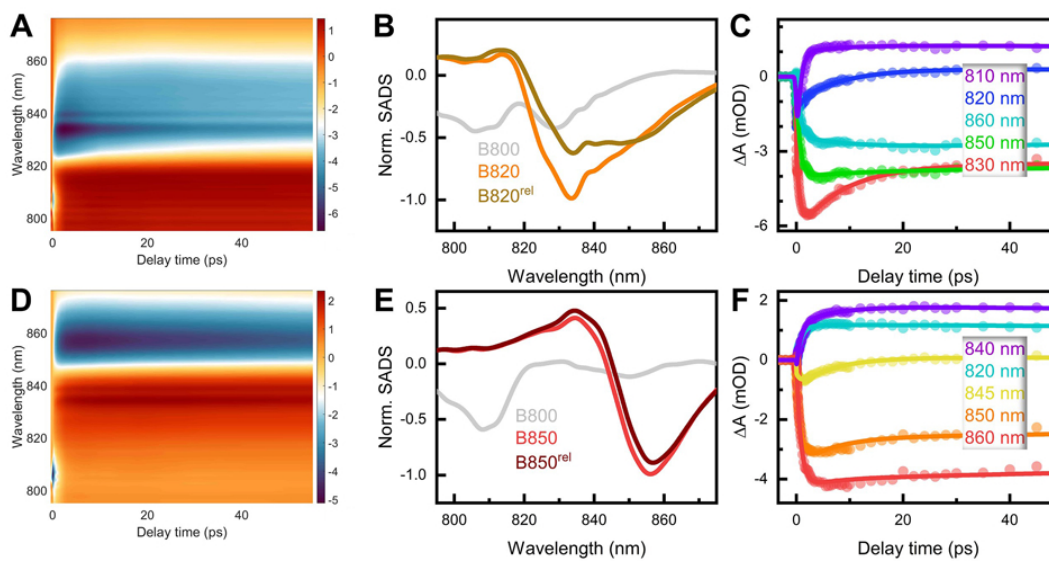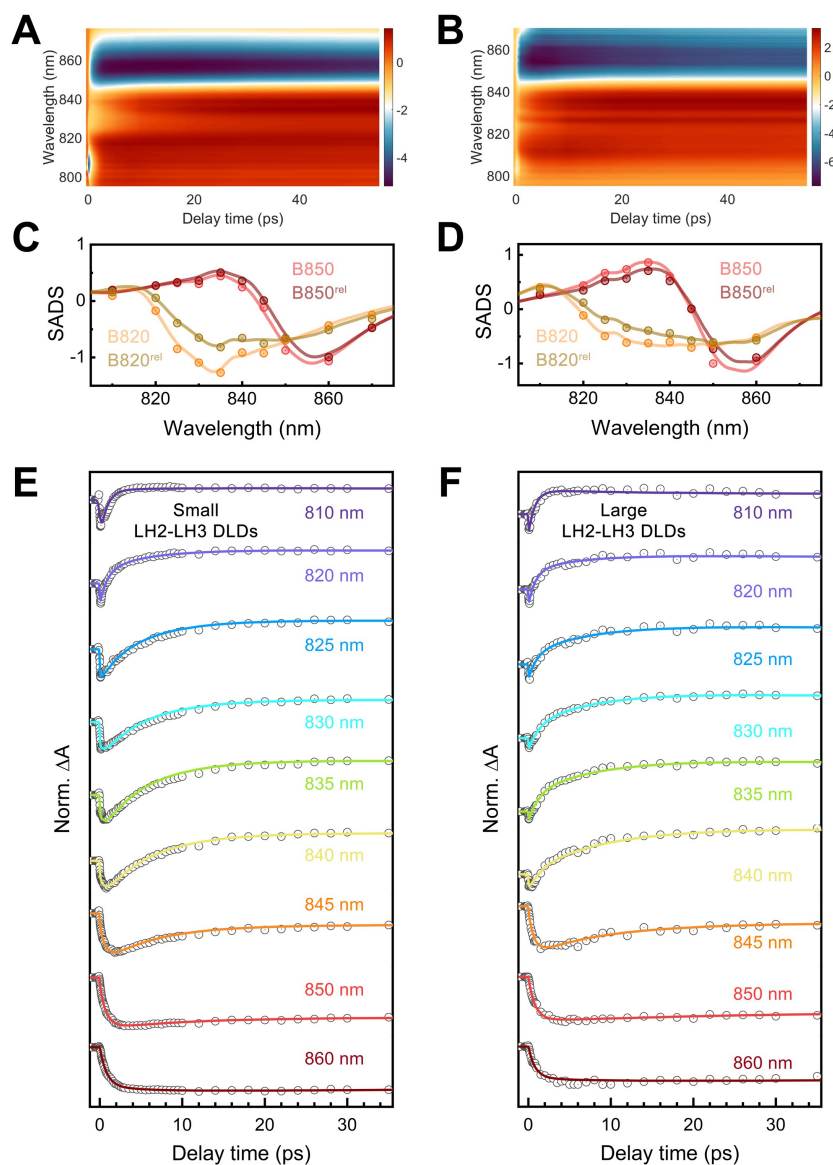
Fig. S15. TA fitting results of LH2-LH3 DLDs samples. 2D representation of the femtosecond-resolved TA spectra of the (A) small and (B) large LH2-LH3 DLDs samples. Color bar describes signal intensity (mOD). (C,D) SADS of B820, B820^{rel}, B850, and B850^{rel} components. Results are shown from both simultaneous fittings of the single-wavelength kinetics (dots) and global analysis (lines). Normalized absorption transients of (E) small and (F) large LH2-LH3 DLDs from 810 to 860 nm. All experimental data are shown as circles, and the best model fits are shown as lines. The timescales are shown in Table S5.

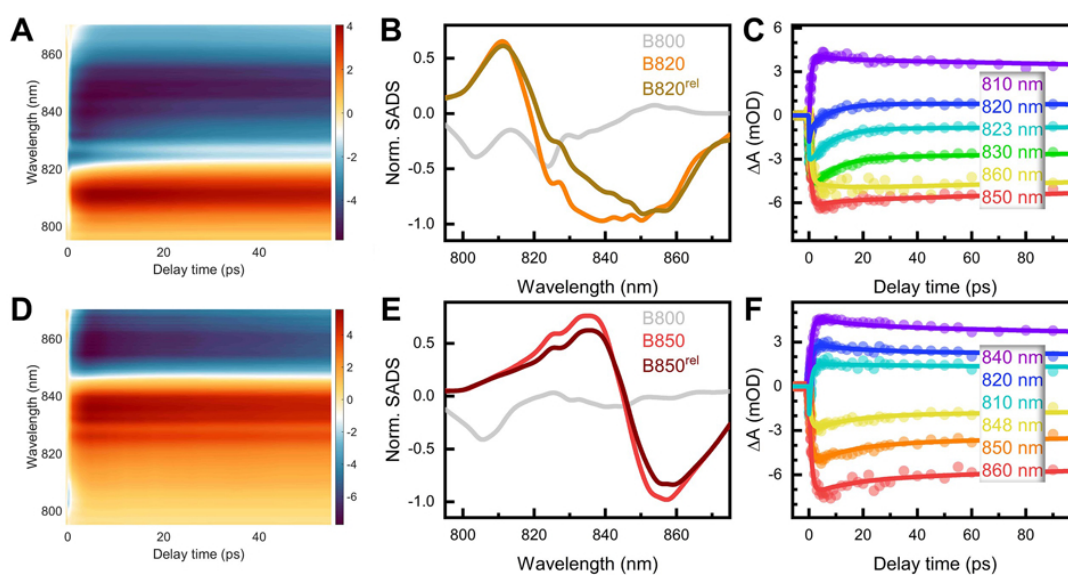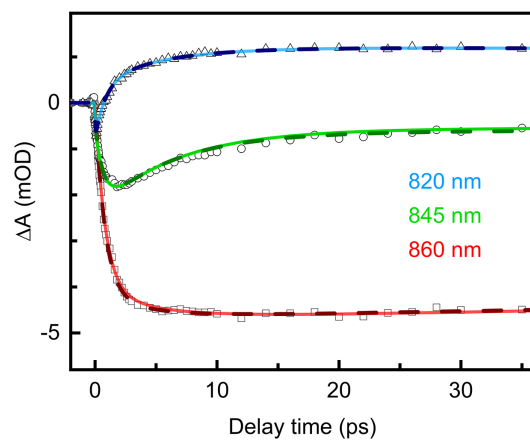**Fig. S16.** TA fitting results of the small LH2-LH3 DLDs sample with one (solid lines) and two (dashed lines) timescale components at selected wavelengths. All experimental data are shown as symbols. The two-component fitting resulted in only a ~10% difference in the timescales (5.5 ps, 85% and 6.1 ps, 15%) compared to the one-component fitting (5.7 ps, 100%).
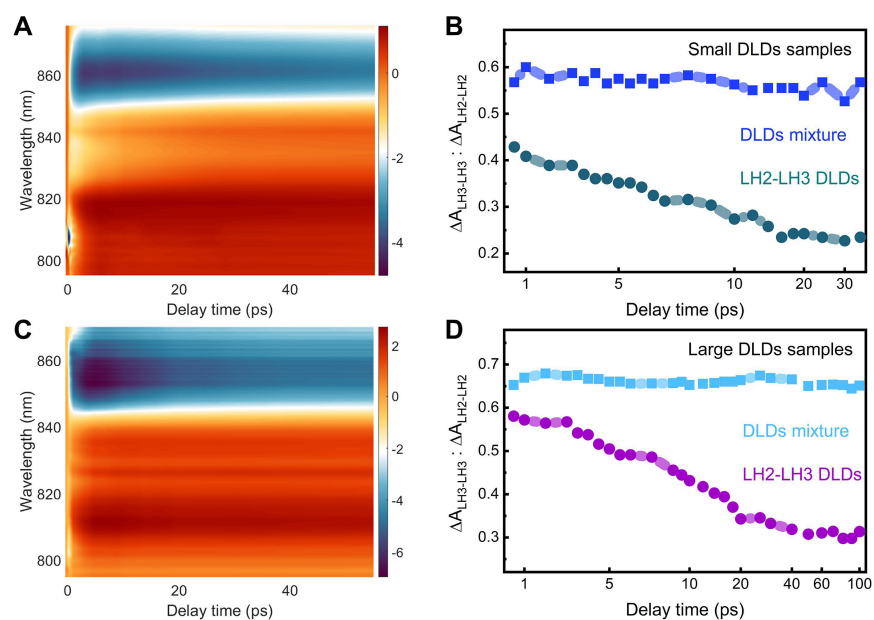
Fig. S17. (A) 2D representation of the femtosecond-resolved TA spectra of the small DLDs mixture and the (B) TA spectral decomposition results. (C) 2D representation of the femtosecond-resolved TA spectra of the large DLDs mixture and the (D) TA spectral decomposition results. Color bar describes signal intensity (mOD). Note that the delay time is shown on a linear scale before 10 ps and a logarithmic scale thereafter.
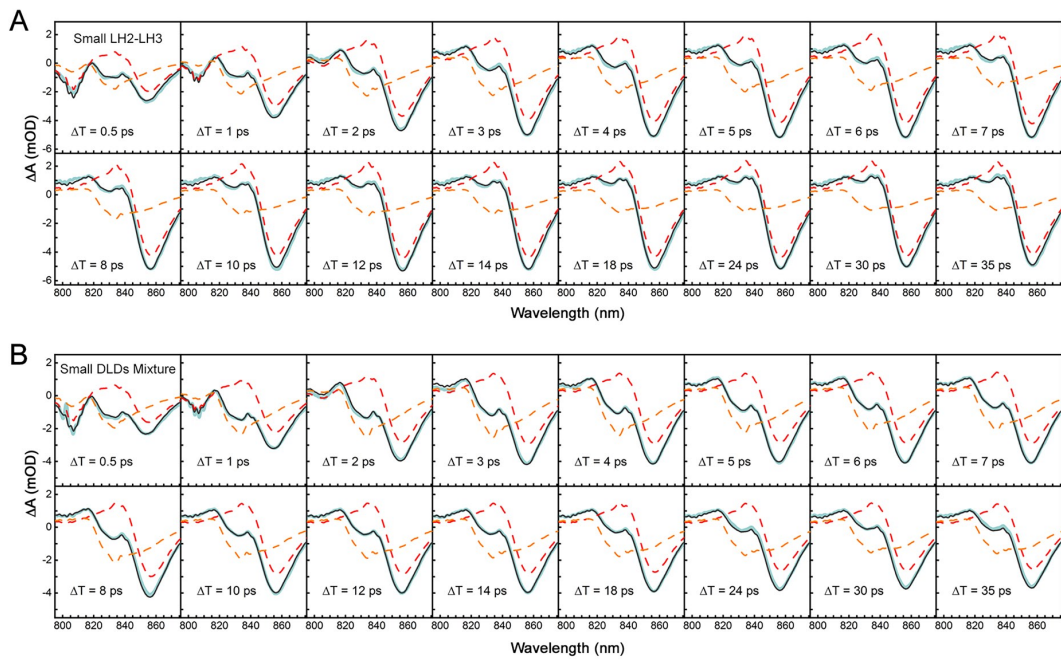
Fig. S18. TA spectral decomposition of (A) small LH2-LH3 DLDs and (B) mixture samples. The dashed lines are the LH2-LH2 (red) and LH3-LH3 (orange) DLDs spectra. The simulated spectra (dark cyan) are in good agreement with the experimentally measured data (turquoise).
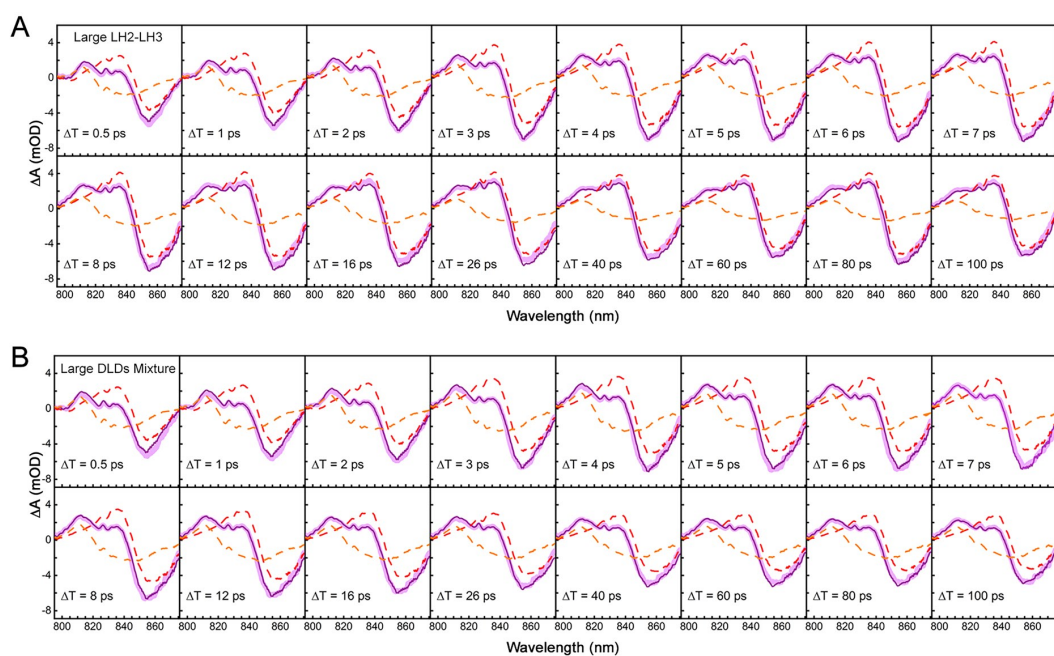
Fig. S19. TA spectral decomposition of (A) large LH2-LH3 DLDs and (B) mixture samples. The dashed lines are the LH2-LH2 (red) and LH3-LH3 (orange) DLDs spectra. The simulated spectra (purple) are in good agreement with the experimentally measured data (lavender).
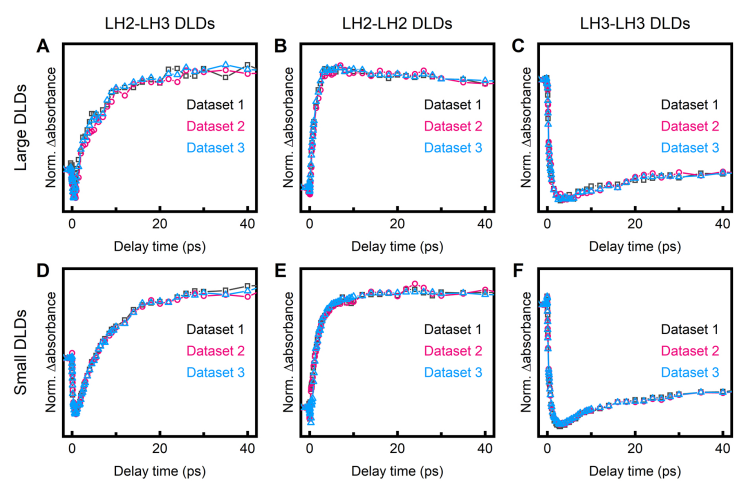
Fig. S20. Reproducibility of the energy transfer dynamics. Overlay of three replicates of the kinetic traces at 840 nm of (A-C) large DLDs and (D-F) small DLDs.
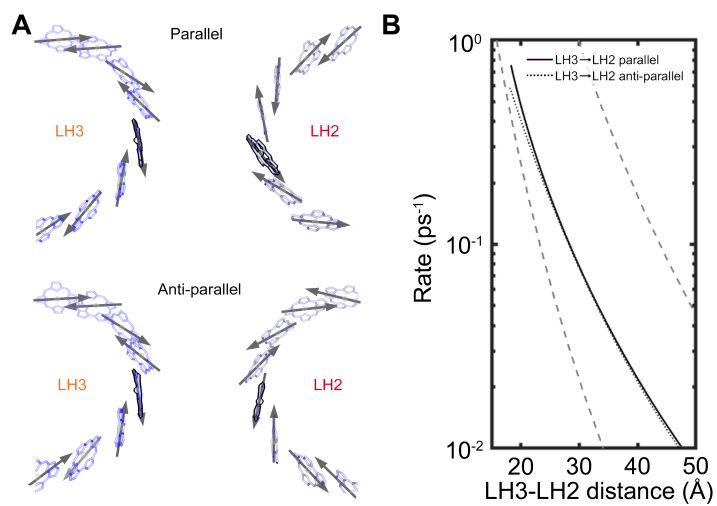
Fig. S21. (A) Transition dipole moments of BChla pigments in parallel (top) and anti-parallel (bottom) orientations in the small DLDs. (B) Theoretical energy transfer rates between the B820 and B850 bands of LH3 and LH2, respectively, in either parallel or anti-parallel orientation, as a function of the distance between the nearest inter-protein BChla pair.
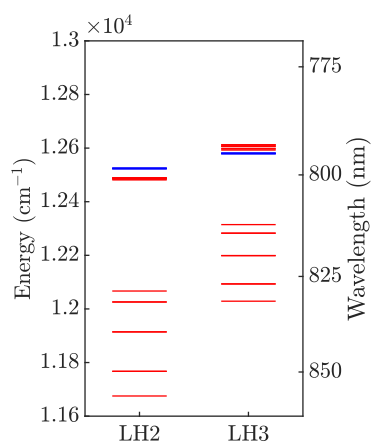
Fig. S22. The excitonic eigenenergies of LH2 (left) and LH3 (right) complexes. The lower band states (B850/B820) are drawn in red and the B800 states are in blue.
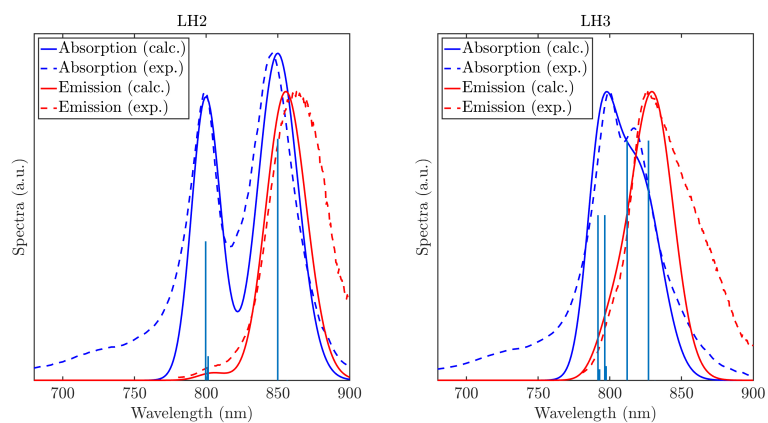
Fig. S23. The calculated linear spectra of LH2 and LH3 complexes (solid), using Eqs. (22) and (23), compared to experiment (dashed). The fluorescence emission is shown in red and the absorption is shown in blue. The stick spectra are also shown.
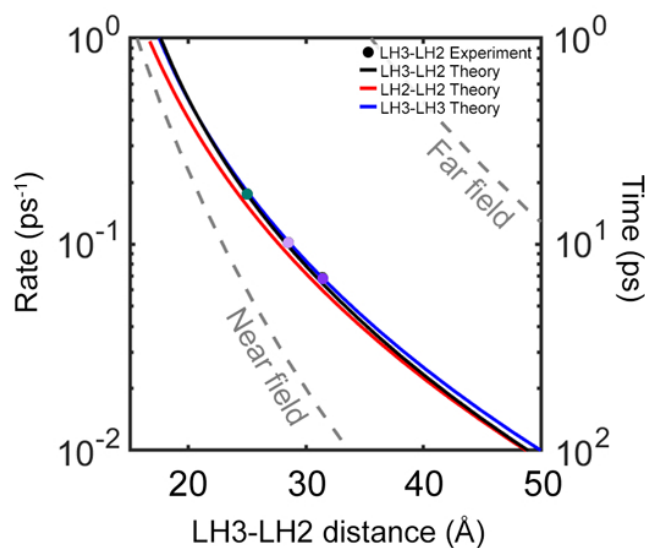
Fig. S24. LH-to-LH energy transfer within the photosynthetic membrane. The rate (left y-axis) and timescale (right y-axis) for inter-protein energy transfer as a function of the LH-LH distance, which was defined as the separation between the nearest B820/B850 and B850 BChla. Energy transfer rates in the far-field (dashed gray line, top) and near-field (dashed gray line, bottom) regimes are also plotted. The experimentally-measured LH3-to-LH2 distances and energy transfer timescales for the small and large DLDs are indicated in teal and two shades of purple dots, respectively. The theoretical generalized FRET rate is indicated by the solid lines - black for LH3-LH2, red for LH2-LH2, and blue for LH3-LH3.

Table S1. Steady-state spectral peak positions of LH2 and LH3 in detergent and DLDs.

Detergent	Abs. peak (nm)	Fluo. peak (nm)
B820	817	826
B850	846	862

DLDs	Abs. peak (nm)	Fluo. peak (nm)
B820	819	834
B850	849	862

Table S2. Spectral decomposition of the steady-state absorption spectra for LH3-LH3 DLDs and LH3-LH3 DLDs high-light. λ is the peak center, %Area is the percent area of each peak, and FWHM is the full width at half maximum. μ is the spectral shape factor in the pseudo-Voigt function representing the fractions of Lorentz (μ) and Gaussian (1-μ) used.

LH3-LH3 DLDs	B850	B820	B800
λ (cm^{-1})	11810	12152	12525
%Area	4.7	47.7	47.6
FWHM (cm^{-1})	331	429	380
μ	0.24	0.91	1.0

LH3-LH3 DLDs High light	B850	B820	B800
λ (cm^{-1})	11810	12152	12525
%Area	10.9	45.6	43.5
FWHM (cm^{-1})	433	480	380
μ	0.24	0.98	1.0

Table S3. Spectral decomposition of the steady-state fluorescence spectra for LH2 and LH3 in detergent and DLDs. λ is the peak position, **%Area is the percent area of each peak, and FWHM is the full width at half maximum.**

LH2 in detergent and DLDs	Peak 1	Peak 2
λ (cm^{-1})	11561	
FWHM (cm^{-1})	625	

LH3 in detergent	Peak 1	Peak 2
λ (cm^{-1})	11632	12099
%Area	46.5	53.5
FWHM (cm^{-1})	674	512

LH3-LH3 DLDs	Peak 1	Peak 2
λ (cm^{-1})	11636	12082
%Area	61.2	38.8
FWHM (cm^{-1})	691	505

Table S4. Spectral decomposition results and population percentage calculations of LH2-LH3 DLDs

	LH2 population[a]	LH3 population[a]	Relative fluorescence[b]
Small LH2-LH3 DLDs	60%	40%	2.67
Large LH2-LH3 DLDs	54%	46%	1.95
Small LH2-LH3 DLDs	LH2-LH2	LH2-LH3	LH3-LH3
Theoretical[c]	36%	48%	16%
Measured	38%	43%	19%
Large LH2-LH3 DLDs	LH2-LH2	LH2-LH3	LH3-LH3
Theoretical[c]	29%	50%	21%
Measured	31%	45%	24%

[a]Total LH2/3 population percentage in the LH2-LH3 DLDs samples based on absorption spectral decomposition.
[b]Relatively integrated fluorescence intensity based on fluorescence spectral decomposition.
[c]Population percentage of DLDs in the LH2-LH3 DLDs sample calculated based on the total population.

Table S5. Timescales extracted from fitting the TA data of LH3 and LH2 in detergent and DLDs.

LH3	τ_1 (ps)	τ_2 (ps)	τ_3 (ns)
Detergent	0.84		1.7
Small DLDs	0.68	8.1	1.5
Large DLDs	0.68	8.1	1.5

LH2	τ_4 (ps)	τ_5 (ps)	τ_6 (ns)
Detergent	1.1		1.5
Small DLDs	0.85	6.6	1.3
Large DLDs	0.85	14.5	1.3

τ_7 (ps)	Parallel	Anti-parallel
Small LH2-LH3 DLDs	5.7	5.7
Large LH2-LH3 DLDs	14.7	9.8

Table S6. On-site energies and intermolecular excitonic couplings for LH2 complexes in wavenumbers.

No.	B800	B850a	B850b
1	12524	-25	3
2	-18	4	19
3	-2	3	-2
4	0	1	-1
5	0	1	0
6	0	1	0
7	-2	2	-1
8	-18	3	-3
9	-25	12377	183
10	3	183	12004
11	3	-61	151
12	-3	16	-36
13	2	-7	12
14	-1	3	-4
15	1	-2	3
16	0	1	-1
17	1	-1	1
18	0	1	-1
19	1	-2	1
20	-1	3	-1
21	3	-7	3
22	-2	12	-4
23	4	-61	16
24	19	151	-36

Table S7. On-site energies and intermolecular excitonic couplings for LH3 complexes in wavenumbers.

No.	B800	B820a	B820b
1	12580	-25	3
2	-18	4	19
3	-2	3	-2
4	0	1	-1
5	0	1	0
6	0	1	0
7	-2	2	-1
8	-18	3	-3
9	-17	12502	162
10	2	161	12289
11	2	-40	92
12	-2	11	-24
13	1	-5	8
14	-1	2	-3
15	1	-2	2
16	0	1	-1
17	1	-1	1
18	0	1	0
19	1	-2	1
20	-1	2	-1
21	2	-5	2
22	-2	8	-3
23	3	-40	11
24	12	92	-24

Table S8. Contribution of lower bands channel to overall energy transfer rate.

Relative Rate	Parallel	Anti-parallel
LH2→LH2	89.99%	98.15%
LH3→LH2	85.04%	97.07%
LH3→LH3	87.02%	95.53%

Table S9. Transport distance of different LH2 arrangements.

Organization	Transport distance (Å)	error (Å)
Uniform	1436.4	0
Cluster	1602.5	1.35
Random	1606.84	1.12

Table S10. Transition monopoles for the BChla Q$_y$ transition

Atom	x coord (Å)	y coord (Å)	z coord (Å)	charge (e⁻)	Atom	x coord (Å)	y coord (Å)	z coord (Å)	charge (e⁻)
Mg	3.07449032	-3.01903914	4.81481524	0.00004688	⋮	⋮	⋮	⋮	⋮
C	3.06449032	-6.16103914	3.44581524	0.00552134	H	0.79664684	-3.83111207	0.36617565	0.00121574
C	1.65249032	-1.67503914	2.02481524	-0.00625652	H	2.75978942	-3.98667936	-1.24905878	0.00248280
C	2.54149032	0.01096086	6.54281524	0.00135922	H	2.67486998	-2.33858926	-0.58208474	-0.00165143
C	4.16849032	-4.43403914	7.83981524	-0.00051531	H	3.87092504	-3.49456583	0.05150593	0.00114703
N	2.46249032	-3.83003914	3.02181524	-0.00204671	H	0.10149033	-5.64017471	0.73904093	-0.00175732
C	2.62149032	-5.13403914	2.58181524	-0.03792793	H	0.97587152	-7.06579516	1.34840988	0.00185594
C	2.27649032	-5.25203914	1.12581524	-0.00141620	H	2.39994856	-7.04924317	-0.54667221	0.00103184
C	1.82549032	-3.87203914	0.72381524	0.00172499	H	1.62868486	-5.56049816	-1.14421490	-0.00134386
C	1.97249032	-3.04303914	1.95881524	0.04973812	H	0.55477823	0.49289393	1.16057447	0.00181956
C	2.86149032	-3.38603914	-0.34518476	0.00119068	H	-0.42922559	1.49232285	2.25654207	0.00252969
C	1.05949032	-6.16003914	0.74781524	-0.00075296	H	1.16771001	2.06740096	1.72049311	0.00250422
C	1.45049032	-6.53103914	-0.68118476	-0.00016126	H	0.42242442	4.27742904	4.87633598	0.00186119
C	0.55949032	-7.34503914	-1.55918476	0.00050763	H	1.15728488	3.59503223	3.40576420	0.00061353
O	0.18449032	-6.89303914	-2.63418476	-0.00171812	H	-0.43077407	3.01243385	3.95976293	0.00062484
O	0.06549032	-8.68803914	-1.35618476	0.00078368	H	2.71150832	-0.59826819	9.31753957	0.00084633
N	2.25349032	-1.18203914	4.39981524	-0.00630098	H	5.09504231	-2.10149953	9.35942723	-0.00181552
C	1.72749032	-0.85603914	3.16581524	0.04666887	H	4.33755851	1.12494537	8.53008158	-0.00191899
C	1.24349032	0.49896086	3.21881524	0.02733226	H	5.05977808	0.16061486	9.84032286	0.00210329
C	1.48449032	0.99396086	4.46781524	0.02112141	H	5.51972317	-0.15005002	8.14910894	0.00069921
C	2.12949032	-0.08403914	5.22681524	0.02339446	H	2.25874114	-2.48183563	10.20822393	-0.00177187
C	0.58549032	1.18896086	1.99881524	0.00205156	H	3.33169258	-3.90164280	10.17373532	0.00215260
C	1.22849032	2.30796086	5.11581524	0.00345402	H	3.30244015	-2.86184832	12.39009706	-0.00024775
O	1.48349032	2.69696086	6.25381524	0.01370291	H	4.91779659	-2.73894557	11.65267917	0.00047328
C	0.54649032	3.37296086	4.28081524	0.00115269	H	3.84484516	-1.31913840	11.68716778	-0.00146188
N	3.33249032	-2.34503914	6.80881524	-0.00164901	H	4.99940737	-6.84651594	8.76919068	-0.00180542
C	3.11149032	-1.03803914	7.26781524	0.03916671	H	4.11893602	-8.28754764	8.20663889	-0.00280533
C	3.54949032	-0.89503914	8.68681524	0.00173550	H	5.77930820	-7.98246612	7.64240829	-0.00272611
C	4.05149032	-2.21503914	9.06581524	-0.00182280	H	2.29579686	-8.21114099	2.93303427	-0.00169831
C	3.86549032	-3.09303914	7.86781524	-0.04522478	H	4.14976667	-9.90243697	-0.67755787	-0.00068587
C	4.70249032	0.13696086	8.81081524	0.00088270	H	4.68171516	-8.20702065	-0.57334179	-0.00069759
C	3.29649032	-2.81403914	10.23681524	-0.00081521	H	5.53280125	-9.46543209	0.35419246	0.00025180
C	3.88249032	-2.40403914	11.58881524	-0.00086734	H	-0.05418552	-9.63157284	-3.21534490	0.00003920
N	3.51749032	-4.85803914	5.54281524	0.00671444	H	-1.33940918	-8.44604046	-2.88220856	-0.00032495
C	3.99349032	-5.28503914	6.75581524	-0.04091635	H	-2.57138660	-9.88689682	-2.31602438	-0.00025463
C	4.28149032	-6.71103914	6.72981524	-0.03346511	H	0.57859387	-11.67646283	-1.12977700	0.00010387
C	3.92549032	-7.12603914	5.45781524	-0.01606366	H	-0.37573813	-12.50493199	0.12368060	0.00021421
C	3.46149032	-5.95203914	4.75281524	-0.02618564	H	-0.18960175	-13.24217832	-1.48569436	-0.00002627
C	4.83549032	-7.51603914	7.92481524	-0.00219625	H	-3.59628632	-11.87844086	-0.93435262	-0.00010145
C	3.83549032	-8.22603914	4.50881524	-0.00492196	H	-2.45677379	-13.04427592	-0.21978529	0.00011802
O	4.11049032	-9.41803914	4.60081524	-0.01565423	H	-2.36518022	-13.40795339	-3.04468684	-0.00002304
C	3.21949032	-7.69503914	3.19481524	-0.00014793	H	-3.01150265	-14.52386741	-1.81779244	0.00003557
C	4.12049032	-7.93703914	2.01581524	0.00002587	H	-5.10900344	-12.77767657	-2.14323355	-0.00000647
O	5.19249032	-7.33803914	1.86581524	-0.00210814	H	-4.41716589	-12.84128358	-3.78200798	-0.00004082
O	3.69949032	-8.93303914	1.05081524	-0.00113895	H	-5.11898552	-15.32157771	-2.13781033	0.00003193
C	4.56249032	-9.13803914	-0.01918476	-0.00008973	H	-3.41207751	-15.69598696	-3.85192767	0.00003961
C	-0.74250968	-9.25403914	-2.45918476	-0.00007033	H	-4.93335034	-16.54377829	-4.21968505	-0.00000364
C	-1.61450968	-10.32103914	-2.02618476	-0.00076873	H	-4.51585088	-15.04747177	-5.08860834	-0.00002870
C	-1.57350968	-11.56403914	-1.43018476	0.00080106	H	-6.88549670	-15.26406221	-4.23410860	-0.00002061
C	-0.29450968	-12.30203914	-0.94418476	0.00015035	H	-6.76790180	-13.53712186	-3.81924099	-0.00002465
C	-2.73050968	-12.51103914	-1.13018476	0.00007396	H	-7.67548446	-13.84497481	-1.69085991	-0.00000728
C	-3.07150968	-13.51303914	-2.22118476	0.00005254	H	-7.20869266	-15.56152385	-1.62896097	0.00002506
C	-4.48550968	-13.35703914	-2.82418476	-0.00007235	H	-9.42478250	-14.36645926	-3.35938438	-0.00002142
C	-5.17450968	-14.74503914	-3.06118476	0.00000687	H	-8.94265510	-16.07981496	-3.34414961	0.00000768
C	-4.44550968	-15.56703914	-4.13218476	-0.00000728	H	-9.97410679	-14.70453039	-0.89262398	0.00000040
C	-6.65350968	-14.55303914	-3.44118476	-0.00003193	H	-8.79249128	-16.89289750	-0.70024706	0.00001132
C	-7.61150968	-14.77103914	-2.26218476	0.00001415	H	-10.50834306	-17.00638849	-0.24063946	-0.00000525
C	-9.01050968	-15.16903914	-2.74918476	-0.00000364	H	-9.97081728	-17.60497551	-1.82841346	0.00000081
C	-10.07150968	-15.45803914	-1.67418476	0.00004163	H	-11.99043351	-16.29132780	-2.01297766	-0.00000081
C	-9.81750968	-16.84003914	-1.06718476	-0.00000121	H	-11.42086933	-15.18456328	-3.28535166	0.00000081
C	-11.51150968	-15.33203914	-2.20918476	-0.00003638	H	-12.41190984	-14.33116369	-0.52852817	0.00000121
C	-12.35750968	-14.20803914	-1.61018476	-0.00000404	H	-11.90147273	-13.24600045	-1.84387656	0.00000081
C	-13.80250968	-14.17803914	-2.14618476	-0.00000485	H	-14.10066454	-13.14576688	-2.32953596	-0.00000647
C	-14.84850968	-14.79103914	-1.17818476	0.00000687	H	-13.85655818	-14.74263232	-3.07699800	-0.00000485
C	-15.10850968	-16.25503914	-1.53418476	0.00000202	H	-14.46319626	-14.74871304	-0.15943942	0.00002263
C	-16.16250968	-13.99803914	-1.25018476	-0.00002546	H	-14.17376549	-16.81325129	-1.48172053	0.00000728
H	1.30813823	-1.15221123	1.13253019	0.00096111	H	-15.82462865	-16.67854992	-0.82997440	-0.00000647
H	2.42962914	0.95141453	7.08238357	0.00083946	H	-15.51249308	-16.31702538	-2.54465748	-0.00000525
H	4.58550647	-4.91711934	8.72346169	-0.00138428	H	-15.97206862	-12.95541519	-0.99569017	-0.00000364
H	3.17859404	-5.65433785	0.66487638	-0.00001172	H	-16.56776124	-14.05729786	-2.26031326	-0.00000485
⋮	⋮	⋮	⋮	⋮	H	-27.25680038	-44.14030710	17.74790339	-0.00000243

References

1. A. L. Tong *et al.*, Comparison of the energy transfer rates in structural and spectral variants of the B800-850 complex from purple bacteria. *J. Phys. Chem. B* **124**, 1460–1469 (2020).

2. J. I. Ogren *et al.*, Impact of the lipid bilayer on energy transfer kinetics in the photosynthetic protein LH2. *Chem. Sci.* **9**, 3095–3104 (2018).

3. M. Son, A. Pinnola, S. C. Gordon, R. Bassi, G. S. Schlau-Cohen, Observation of dissipative chlorophyll-to-carotenoid energy transfer in light-harvesting complex II in membrane nanodiscs. *Nat. Commun.* **11**, 1295 (2020).

4. J. Zivanov *et al.*, New tools for automated high-resolution cryo-EM structure determination in RELION-3. *eLife* **7**, e42166 (2018).

5. A. Rohou, N. Grigorieff, CTFFIND4: Fast and accurate defocus estimation from electron micrographs. *J. Struc. Biol.* **192**, 216–221 (2015).

6. T. D. Goddard *et al.*, UCSF ChimeraX: Meeting modern challenges in visualization and analysis. *Protein Sci.* **27**, 14–25 (2018).

7. L. Wang *et al.*, Interfacial trap-assisted triplet generation in lead halide perovskite sensitized solid-state upconversion. *Adv. Mater.* **33**, 2100854 (2021).

8. J. R. Lakowicz, *Principles of fluorescence spectroscopy.* (Springer), (2006).

9. B. Brüggemann, J. L. Herek, V. Sundström, T. Pullerits, V. May, Microscopic theory of exciton annihilation: Application to the LH2 antenna system. *J. Phys. Chem. B* **105**, 11391–11394 (2001).

10. S. A. Kovalenko, A. L. Dobryakov, J. Ruthmann, N. P. Ernsting, Femtosecond spectroscopy of condensed phases with chirped supercontinuum probing. *Phys. Rev. A* **59**, 2369 (1999).

11. J. J. Snellenburg, S. P. Laptenok, R. Seger, K. M. Mullen, I. H. van Stokkum, Glotaran: A java-based graphical user interface for the R package TIMP. *J. Stat. Softw.* **49**, 1–22 (2012).

12. J. Chmeliov *et al.*, Excitons in the LH3 complexes from purple bacteria. *J. Phys. Chem. B* **117**, 11058–11068 (2013).

13. K. Sauer, K. D. Philipson, S. C. Tsai, Circular dichroism of chlorophyll and related molecules calculated using a point monopole model for the electronic transitions. *J. Phys. Chem.* **75**, 1440–1445 (1971).

14. J. C. Chang, Monopole effects on electronic excitation interactions between large molecules. I. application to energy transfer in chlorophylls. *J. Chem. Phys.* **67**, 3901–3909 (1977).

15. M. J. Frisch *et al.*, Gaussian~16 Revision C.01 (2016) Gaussian Inc. Wallingford CT.

16. L. Cleary, J. Cao, Optimal thermal bath for robust excitation energy transfer in disordered light-harvesting complex 2 of purple bacteria. *New J. Phys.* **15**, 125030 (2013).

17. J. Ma, J. Cao, Förster resonance energy transfer, absorption and emission spectra in multichromophoric systems. I. Full cumulant expansions and system-bath entanglement. *J. Chem. Phys.* **142**, 094106 (2015).

18. J. Strümpfer, K. Schulten, Light harvesting complex II B850 excitation dynamics. *J. Chem. Phys.* **131**, 225101 (2009).